Vietnam Journal of Mechanics, Vietnam Academy of Science and Technology
DOI: https://doi.org/10.15625/0866-7136/23994

# NONLINEAR BUCKLING ANALYSIS OF POROUS-CORE FG-GPLRC TOROIDAL SHELL SEGMENTS WITH GENERALIZED MERIDIONAL CURVATURE REINFORCED BY ORTHOGONAL STIFFENERS

**Vu Hoai Nam**[1], **Kieu Lan Huong**[1,2], **Le Ngoc Ly**[1], **Cao Van Doan**[1,*], **Pham Thanh Hieu**[1]
[1]*Mechanics of Advanced Materials and Structures, University of Transport Technology, Hanoi, Vietnam*
[2]*Graduate University of Science and Technology, Vietnam Academy of Science and Technology, Hanoi, Vietnam*
E-mail: doancv@utt.edu.vn

Received: 22 December 2025 / Revised: 05 January 2026 / Accepted: 10 January 2026
Published online: 10 March 2026

**Abstract.** By utilizing the Donnell shell theory with von Kármán strain-displacement relationship, the nonlinear buckling behavior of porous core functionally graded graphene platelet-reinforced composite (FG-GPLRC) toroidal shell segments with generalized meridional curvature reinforced by stiffeners subjected to external pressure is introduced in this paper. Orthogonal FG-GPLRC stiffeners are applied on the bottom surface to enhance the load-carrying capacity of the shells. An improved smeared stiffener technique is employed for the FG-GPLRC stiffeners, while a three-term solution form is selected to satisfy the simply supported boundary conditions. The Ritz method is used to determine the explicit expressions for the critical buckling load and the load-deflection postbuckling curve of the shells. Numerical results reveal that both the stiffener configuration and the porous core thickness significantly influence the critical and postbuckling loads. Additionally, the effects of graphene distribution and geometric parameters on the nonlinear buckling behavior of stiffened FG-GPLRC toroidal shell segments are analyzed in detail.

*Keywords*: functionally graded graphene platelet reinforced composite (FG-GPLRC), nonlinear buckling analysis, Donnell shell theory, toroidal shell segments, porous core.

## 1. INTRODUCTION

Functionally graded material (FGM) has attracted increasing attention in recent decades due to its superior properties under complex loading and environmental conditions. These materials have been applied in a wide range of engineering fields, such as aerospace engineering, spacecraft structures, nuclear fusion systems, and medical technology (Klecka et al., 2023; Shi et al., 2021; Yadav et al., 2024). The behavior of FGM structures subjected to mechanical loads in a thermal environment has been studied by many authors. For instance, based on a higher-order shear deformation shell theory (HSDT) with von Kármán nonlinearity, the postbuckling behavior of FGM cylindrical shells was studied by Shen and Noda (2005), under combined axial compressive load and external pressure in thermal environments. Additionally, Naj et al. (2008) used the first-order shear deformation shell theory (FSDT) and the Sanders nonlinear kinematics equations to explore the thermal and mechanical instability of FGM truncated conical shells, contributing to the understanding of their buckling behavior under various loading conditions.

Functionally Graded Carbon Nanotube-Reinforced Composite (FG-CNTRC) has attracted considerable interest because of its exceptional mechanical and thermal properties, which make

it highly suitable for applications under complex loading conditions. Based on HSDT and Hamilton's principle, buckling and vibration analysis of FG-CNTRC rectangular plates were studied by Cheshmeh et al. (2020). The results showed that the FG-X pattern of CNT distribution, and the increase of CNT volume fraction, led to an increase in the buckling loads of the FG-CNTRC plates. By using the FSDT and considering the surrounding elastic media as well as the tangential elasticity of edges, Hieu and Tung (2020) studied the thermal and mechanical buckling behavior of FG-CNTRC toroidal shell segments through the Galerkin method. Based on HSDT and the Galerkin method, Minh et al. (2022) studied the nonlinear buckling behavior of FG-CNTRC plates stiffened by oblique FG-CNTRC stiffeners.

Plate and shell structures made from two types of graphene-reinforced composites, namely, functionally graded graphene-reinforced composites (FG-GRCs) and functionally graded graphene platelet-reinforced composites (FG-GPLRCs), have also attracted significant research interest from scientists. Based on the Donnell shell theory with the Stein and McElman approximation, considering the anisotropic smeared FG-GRC stiffener technique, the von Kármán geometrical nonlinearity, and the Pasternak foundation model, the torsional buckling and postbuckling behavior of stiffened FG-GRC toroidal shell segments was studied by Doan et al. (2022). Nguyen et al. (2021) and Phuong et al. (2020) investigated and analyzed the effects of the stiffeners on the nonlinear thermo-mechanical buckling behavior of FG-GRC cylindrical shells subjected to external pressure and torsional load, respectively. The results showed the significant effects of the stiffeners on the postbuckling curves and the critical buckling loads. Zhang et al. (2023) used a Navier-type solution to investigate the temperature-dependent thermo-mechanical responses of porous FG-GPLRC cylindrical panels subjected to an initial blast pressure. By taking into account the pre-buckling effects and in-plane constraint, the nonlinear axially compressive buckling behavior of a porous FG-GPLRC cylindrical shell was analyzed by Zhou et al. (2019).

This paper presents the design and analysis of porous core FG-GPLRC toroidal shell segments with generalized meridional curvature, stiffened by orthogonal stiffeners, and subjected to external pressure. The functionally graded or uniform distributions of graphene platelet (GPL) are designed along the thickness of both face sheets; additionally, the porosity in the shell is symmetrically distributed. Donnell shell theory and the smeared stiffener technique, incorporating von Kármán geometric nonlinearity, are used. The Ritz method is applied to derive explicit expressions for the critical buckling load and the load-deflection postbuckling curve. The numerical results demonstrate the significant influence of the stiffeners' properties, GPL distribution, and geometric parameters on the nonlinear buckling behavior of stiffened FG-GPLRC toroidal shell segments with a porous core.

## 2. GEOMETRICAL CONFIGURATION AND MATERIAL PROPERTIES OF POROUS CORE STIFFENED FG-GPLRC TOROIDAL SHELL SEGMENTS

Fig. 1 illustrates the porous core stiffened FG-GPLRC toroidal shell segments within the $Oxyz$ coordinate system, with the origin located at the shell's mid-surface. The thickness and porosity coefficient of the porous core are $h_{Core}$ and $e_0$. The letters $L$, $a$ and $h = h_{Core} + 2h_{GPL}$ are the length, average radius, and thickness of the shell, respectively. The height, the width, and the spacing of the stiffener system are respectively denoted by $h_{St}$, $b_{St}$, and $d_{St}$. $n_S$ and $n_R$ are the numbers of stiffeners in the meridional and circumferential directions, respectively. In this paper, meridional parabolic, half-sinusoidal, and circular profiles are considered, as they represent typical geometries frequently employed in engineering shell design. The equations of the meridional curve in the cases of the parabolic and half-sinusoid shells are determined by the following expressions

$$g_{(Pa-x)} = \frac{4\,(x-L)\,x}{L^2}H, \quad g_{(Si-x)} = H\sin\left(-\frac{\pi x}{L}\right), \tag{1}$$

where $H$ is the rise of the shell.

From Eq. (1), meridional radii of the two shell types are derived using the standard formula for the radius of curvature of a planar curve, as

$$\begin{aligned} R_{(Pa-x)} &= \frac{1}{8L^4H}\left[L^4+16H^2\left(L-2x\right)^2\right]^{3/2}, \\ R_{(Si-x)} &= \frac{\sin^{-1}\left(x\pi/L\right)}{LH\pi^2}\left\{\left[\cos\left(\frac{2\pi x}{L}\right)+1\right]\frac{L^2H^2\pi^2}{2}\right\}^{3/2}. \end{aligned} \tag{2}$$

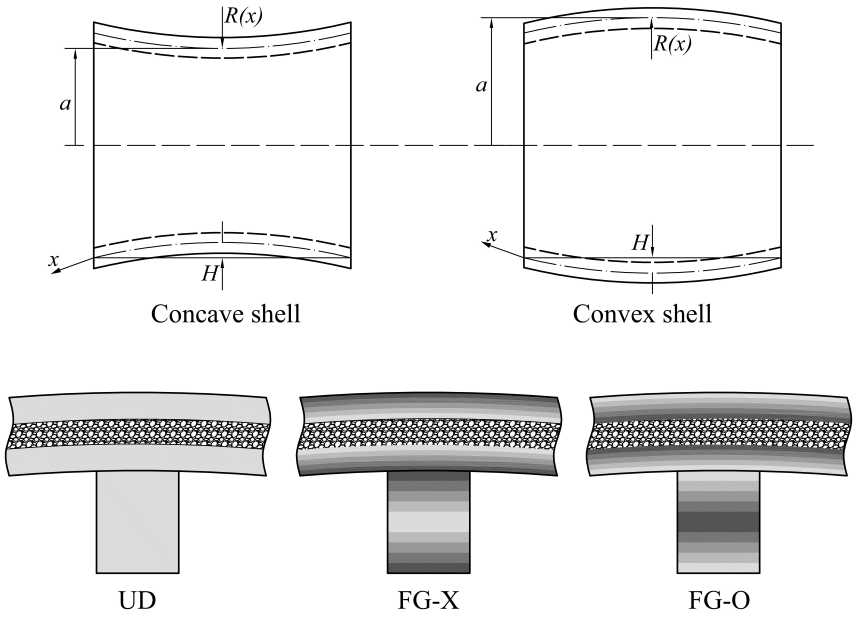


*Fig. 1.* Geometry, coordinate system, and GPL distribution of stiffened FG-GPLRC toroidal shell segments with porous core

The porosity distribution along the thickness direction is assumed to be symmetric; therefore, the Young's modulus of the porous core can be expressed as

$$E_{Core} = E_{11Core} = E_{22Core} = E_m\left[1-e_0\cos\left(\frac{\pi z}{h_{Core}}\right)\right]. \tag{3}$$

Based on the extended model of Halpin-Tsai micromechanics, the Young's modulus of the composite with randomly oriented GPLs is calculated by (Wang et al., 2020)

$$E_{COM} = \frac{5}{8}\left(\frac{1+\eta_T\xi_T V_{GPL}}{1-V_{GPL}\eta_T}\right)E_m + \frac{3}{8}\left(\frac{1+\eta_L\xi_L V_{GPL}}{1-V_{GPL}\eta_L}\right)E_m, \tag{4}$$

where $E_m$ is Young's modulus of the polymer matrix; $\eta_L, \eta_T, \xi_L, \xi_T$ and $V_{GPL}$ are described by (Wang et al., 2020)

$$\xi_L = \frac{2a_{GPL}}{h_{GPL}}, \quad \eta_L = \frac{E_{GPL}/E_m - 1}{E_{GPL}/E_m + \xi_L}, \quad \eta_T = \frac{E_{GPL}/E_m - 1}{E_{GPL}/E_m + \xi_T}, \quad \xi_T = \frac{2b_{GPL}}{h_{GPL}}, \tag{5}$$

$$V_{GPL} = \frac{\bar{W}_{GPL}}{\bar{W}_{GPL} + \frac{\rho_{GPL}}{\rho_m}\left(1-\bar{W}_{GPL}\right)}, \tag{6}$$

in which $a_{GPL} = 2.5$ μm, $b_{GPL} = 1.5$ μm, $h_{GPL} = 1.5$ nm, and $E_{GPL}$ are the length, width, thickness and Young's modulus of the GPLs, respectively. $\bar{W}_{GPL}$ is the mass fraction of GPLs

depending on the thickness of the shell and stiffeners, and is designed according to the three considered distribution patterns of GPLs.

For the stiffened shell, three corresponding distribution patterns of GPLs are assumed as

$$\text{UD shell } (\bar{W}_{GPL} = W^*_{GPL}) \text{ with UD stiffeners } (\bar{W}_{GPL} = W^*_{GPL}) \tag{7}$$

$$\text{FG-X shell } \left(\bar{W}_{GPL} = \frac{4|z|}{h} W^*_{GPL}\right) \text{ with FG-X stiffeners } \left(\bar{W}_{GPL} = \left(\left|\frac{2h-4z}{h_{St}}\right| + 2\right) W^*_{GPL}\right) \tag{8}$$

$$\text{FG-O shell } \left(\bar{W}_{GPL} = \left(2 - \frac{4|z|}{h}\right) W^*_{GPL}\right) \text{ with FG-O stiffeners } \left(\bar{W}_{GPL} = \left(2 - \left|\frac{4z-2h}{h_{St}} - 2\right|\right) W^*_{GPL}\right) \tag{9}$$

where $z$ is defined in the range $h/2 \le z \le h/2 + h_{St}$ for the stiffeners, and $-h/2 \le z \le h/2$ for the shell skin, and $W^*_{GPL}$ is the total GPL mass fraction.

The density and effective Poisson's ratio according to the mixture rule are expressed by

$$\rho_{COM} = \rho_{GLP} V_{GLP} + \rho_m V_m, \quad v_{COM} = v_{GLP} V_{GPL} + v_m V_m, \tag{10}$$

where $v_{GLP}$ and $v_m$ are the Poisson's ratios of the GPLs and polymer matrix, respectively. The properties of FG-GPLRC in this paper are selected similarly to the study (Wang et al., 2020).

## 3. MATHEMATICAL FORMULATIONS

The Donnell theory used in this study is based on the standard assumptions for thin shells with moderate curvature variations, namely, with a sufficiently large $a/h$ ratio. Strain components at the distance $z$ from the mid-surface are written as

$$\gamma_{xy} = \gamma_{0xy} - 2zw_{,xy}, \quad \varepsilon_x = \varepsilon_{0x} - zw_{,xx}, \quad \varepsilon_y = \varepsilon_{0y} - zw_{,yy}, \tag{11}$$

where $\gamma_{0xy}$ is the shear strain, $\varepsilon_{0x}$ and $\varepsilon_{0y}$ are the normal strains at the mid-plane of the shell, and

$$\gamma_{0xy} = w_{,x}w_{,y} + v_{,x} + u_{,y}, \quad \varepsilon_{0x} = u_{,x} + \frac{w^2_{,x}}{2} - \frac{w}{R}, \quad \varepsilon_{0y} = v_{,y} + \frac{w^2_{,y}}{2} - \frac{w}{a}. \tag{12}$$

The deformation compatibility equation is obtained from Eq. (12) as

$$\varepsilon_{0x,yy} - \gamma_{0xy,xy} + \varepsilon_{0y,xx} = w^2_{,xy} - \frac{w_{,yy}}{R} - w_{,yy}w_{,xx} - \frac{w_{,xx}}{a}. \tag{13}$$

Relationship expressions between stresses and strains of the shell are determined by

$$\begin{Bmatrix} \sigma_x \\ \sigma_y \\ \sigma_{xy} \end{Bmatrix} = \begin{bmatrix} Q_{11} & Q_{12} & 0 \\ Q_{21} & Q_{22} & 0 \\ 0 & 0 & Q_{66} \end{bmatrix} \begin{bmatrix} \varepsilon_x \\ \varepsilon_y \\ \gamma_{xy} \end{bmatrix}, \tag{14}$$

where $Q_{ij}$ $(i, j = 1, 2, 6)$ is determined depending on the material, with the FG-GPLRC layer

$$Q_{11} = Q_{22} = \frac{E_{COM}}{1 - \nu^2_{COM}}, \quad Q_{12} = Q_{21} = \frac{\nu_{COM} E_{COM}}{1 - \nu^2_{COM}}, \quad Q_{66} = \frac{E_{COM}}{2(1 + \nu_{COM})}, \tag{15}$$

and with the core layer

$$Q_{11} = Q_{22} = \frac{E_{Core}}{1 - \nu^2_{Core}}, \quad Q_{12} = Q_{21} = \frac{\nu_{Core} E_{Core}}{1 - \nu^2_{Core}}, \quad Q_{66} = \frac{E_{Core}}{2(1 + \nu_{Core})}. \tag{16}$$

The smeared anisotropic stiffener technique for FG-GPLRC stiffeners is developed according to the idea of classical Lekhnitskii's smeared stiffener technique. By integrating the stresses through the thickness of the shell skin, and combining with the improved smeared stiffener technique, the forces and moments of the FG-GPLRC shell with porous core stiffened by meridional, circumferential FG-GPLRC stiffeners are expressed as

$$\left\{\begin{array}{c} N_x \\ N_y \\ N_{xy} \\ M_x \\ M_y \\ M_{xy} \end{array}\right\} = \left\{\begin{array}{cccccc} A_{11} & A_{12} & 0 & B_{11} & B_{12} & 0 \\ A_{21} & A_{22} & 0 & B_{21} & B_{22} & 0 \\ 0 & 0 & A_{66} & 0 & 0 & B_{66} \\ B_{11} & B_{12} & 0 & D_{11} & D_{12} & 0 \\ B_{21} & B_{22} & 0 & D_{21} & D_{22} & 0 \\ 0 & 0 & B_{66} & 0 & 0 & D_{66} \end{array}\right\} \left\{\begin{array}{c} \varepsilon_{0x} \\ \varepsilon_{0y} \\ \gamma_{0xy} \\ -w_{,xx} \\ -w_{,yy} \\ -2w_{,xy} \end{array}\right\}, \tag{17}$$

where $A_{ij}, B_{ij}, D_{ij}\,(i,j=1,2,6)$ are the stiffnesses of the stiffened FG-GPLRC toroidal shell segments with porous core, and

$$\begin{gathered} A_{11} = A_{11SH} + \chi_1\xi_A, \quad A_{22} = A_{22SH} + \chi_2\xi_A, \quad A_{12} = A_{12SH}, \quad A_{66} = A_{66SH}, \quad \xi_A = \frac{b_{St}}{d_{St}}A_{11St}, \\ B_{11} = B_{11SH} + \chi_1\xi_B, \quad B_{22} = B_{22SH} + \chi_2\xi_B, \quad B_{12} = B_{12SH}, \quad B_{66} = B_{66SH}, \quad \xi_B = \frac{b_{St}}{d_{St}}B_{11St}, \\ D_{11} = D_{11SH} + \chi_1\xi_D, \quad D_{22} = D_{22SH} + \chi_2\xi_D, \quad D_{12} = D_{12SH}, \quad D_{66} = D_{66SH}, \quad \xi_D = \frac{b_{St}}{d_{St}}D_{11St}, \end{gathered} \tag{18}$$

with $\chi_1 = 1, \chi_2 = 0$ is defined for the meridionally stiffened shells, $\chi_1 = 0, \chi_2 = 1$ for the circumferentially stiffened shells, $\chi_1 = \chi_2 = 1$ for the orthogonally stiffened shells, and $\chi_1 = \chi_2 = 0$ for the unstiffened shell, and

$$\begin{gathered} \left(A_{ijSH}, B_{ijSH}, D_{ijSH}\right)_{(k)} = \sum_{k=1}^{11} \int_{\Pi(k)} Q_{ij(k)}\left(1, z, z^2\right) \mathrm{d}z, \quad (i,j=1,2,6), \\ \left[\begin{array}{cc} A_{11St} & B_{11St} \\ B_{11St} & D_{11St} \end{array}\right] = \sum_{k=1}^{10} \left( \left[\begin{array}{cc} \bar{A}_{11} & \bar{B}_{11} \\ \bar{B}_{11} & \bar{D}_{11} \end{array}\right] - MT_A\, MT_B \left[\begin{array}{cc} \bar{A}_{12} & \bar{B}_{12} \\ 0 & 0 \\ \bar{B}_{12} & \bar{D}_{12} \\ 0 & 0 \end{array}\right] \right), \\ MT_A = \left[\begin{array}{cccc} \bar{A}_{12} & 0 & \bar{B}_{12} & 0 \\ \bar{B}_{12} & 0 & \bar{D}_{12} & 0 \end{array}\right], \quad MT_B = \left[\begin{array}{cccc} \bar{A}_{22} & 0 & \bar{B}_{22} & 0 \\ 0 & \bar{A}_{66} & 0 & \bar{B}_{66} \\ \bar{B}_{22} & 0 & \bar{D}_{22} & 0 \\ 0 & \bar{B}_{66} & 0 & \bar{D}_{66} \end{array}\right]^{-1}, \end{gathered} \tag{19}$$

where $\Pi(k)$ are the domains of integration in the thickness direction, and

$$\left(\bar{A}_{ij}, \bar{B}_{ij}, \bar{D}_{ij}\right)_{(k)} = \int_{\Delta(k)} Q_{ij(k)}\left(1, z, z^2\right) \mathrm{d}z, \quad (i,j=1,2,6). \tag{20}$$

with $\Delta(k)$ is the domain of integration in the thickness direction of the stiffener.

From Eq. (17), we have

$$\begin{aligned} \gamma_{0xy} &= 2w_{,xy}B^*_{66} + N_{xy}A^*_{66}, \\ \varepsilon_{0x} &= N_yA^*_{12} + B^*_{12}w_{,yy} + B^*_{11}w_{,xx} + N_xA^*_{11}, \\ \varepsilon_{0y} &= N_yA^*_{22} + B^*_{22}w_{,yy} + B^*_{21}w_{,xx} + N_xA^*_{21} \end{aligned} \tag{21}$$

$$\begin{aligned} M_{xy} &= 2S_{66}w_{,xy} + N_{xy}X_{66}, \\ M_x &= N_yX_{12} + S_{12}w_{,yy} + S_{11}w_{,xx} + N_xX_{11}, \\ M_y &= N_yX_{22} + S_{22}w_{,yy} + S_{21}w_{,xx} + N_xX_{21} \end{aligned} \tag{22}$$

where

$$A_{21}^{*}=-\frac{A_{21}}{\kappa_1},\quad A_{11}^{*}=\frac{A_{22}}{\kappa_1},\quad B_{22}^{*}=\frac{B_{22}A_{11}-A_{21}B_{12}}{\kappa_1},\quad B_{21}^{*}=\frac{B_{21}A_{11}-A_{21}B_{11}}{\kappa_1},\quad B_{66}^{*}=\frac{B_{66}}{A_{66}},$$
$$A_{66}^{*}=A_{66}^{-1},\quad A_{12}^{*}=-\frac{A_{12}}{\kappa_1},\quad A_{22}^{*}=\frac{A_{11}}{\kappa_1},\quad B_{12}^{*}=\frac{A_{22}B_{12}-B_{22}A_{12}}{\kappa_1},\quad B_{11}^{*}=\frac{B_{11}A_{22}-A_{12}B_{21}}{\kappa_1},$$
$$\kappa_1=A_{11}A_{22}-A_{12}A_{21}, X_{12}=B_{11}A_{12}^{*}+B_{12}A_{22}^{*}, X_{22}=B_{21}A_{12}^{*}+A_{22}^{*}B_{22}, X_{11}=B_{11}A_{11}^{*}+A_{21}^{*}B_{12},$$
$$S_{12}=B_{12}^{*}B_{11}-D_{12}+B_{12}B_{22}^{*},\quad S_{22}=B_{21}B_{12}^{*}-D_{22}+B_{22}^{*}B_{22},\quad S_{11}=B_{11}B_{11}^{*}-D_{11}+B_{12}B_{21}^{*},$$
$$X_{21}=A_{11}^{*}B_{21}+B_{22}A_{21}^{*},\quad S_{66}=B_{66}^{*}B_{66}-D_{66},\quad S_{21}=B_{21}B_{11}^{*}-D_{21}+B_{22}B_{21}^{*},\quad X_{66}=A_{66}^{*}B_{66}$$

The stress function $f(x,y)$ satisfying the following conditions can be presented as

$$N_{xy}=-f_{,xy}, N_x=f_{,yy}, N_y=f_{,xx}. \tag{23}$$

The compatibility equation is rewritten when substituting Eqs. (17), (23) into Eq. (13) as

$$\beta\equiv A_{22}^{*}f_{,xxxx}+T_1f_{,xxyy}+A_{11}^{*}f_{,yyyy}+B_{12}^{*}w_{,yyyy}+T_2w_{,xxyy}+B_{21}^{*}w_{,xxxx}+w_{,xx}\left(\frac{1}{a}+w_{,yy}\right)$$
$$+\frac{1}{R}w_{,yy}-\left(w_{,xy}\right)^2=0,\quad T_1=\left(A_{12}^{*}+A_{66}^{*}+A_{21}^{*}\right),\quad T_2=\left(B_{11}^{*}-2B_{66}^{*}+B_{22}^{*}\right). \tag{24}$$

A three-term solution form is selected to ensure deflection satisfies the simply supported boundary condition, as

$$w=\alpha_0+\alpha_1\sin\left(\frac{m\pi x}{L}\right)\sin\left(\frac{ny}{R}\right)+\alpha_2\sin\left(\frac{m\pi x}{L}\right)^2, \tag{25}$$

where $\alpha_0$, $\alpha_1$ and $\alpha_2$ are respectively the uniform amplitude of the prebuckling state, the linear and nonlinear buckling amplitudes; $m$ and $n$ respectively are the half-wave numbers in the meridional direction and wave numbers in the circumferential direction.

The expression of the stress function of circular toroidal shell segments can be determined when substituting Eq. (25) into Eq. (24), obtained as

$$f=f_1\cos\left(\frac{2m\pi x}{L}\right)+f_2\cos\left(\frac{2ny}{a}\right)+f_3\sin\left(\frac{m\pi x}{L}\right)\sin\left(\frac{ny}{a}\right)+f_4\sin\left(\frac{3m\pi x}{L}\right)\sin\left(\frac{ny}{a}\right)-\frac{\sigma_{oy}hx^2}{2}, \tag{26}$$

where $\sigma_{oy}$ is the average circumferential stress of the shell.

In the case of parabolic and half-sinusoid shell segments, the coefficients of the stress function can be obtained by calculating the following integrals

$$\int_0^L\int_0^{2\pi a}\beta\cos\left(\frac{2m\pi x}{L}\right)\mathrm{d}y\mathrm{d}x=0,\quad \int_0^L\int_0^{2\pi a}\beta\cos\left(\frac{2ny}{a}\right)\mathrm{d}y\mathrm{d}x=0,$$
$$\int_0^L\int_0^{2\pi a}\beta\sin\left(\frac{ny}{a}\right)\sin\left(\frac{m\pi x}{L}\right)\mathrm{d}y\mathrm{d}x=0,\quad \int_0^L\int_0^{2\pi a}\beta\sin\left(\frac{ny}{a}\right)\sin\left(\frac{3m\pi x}{L}\right)\mathrm{d}y\mathrm{d}x=0. \tag{27}$$

From Eq. (27), we have

$$f_1=u_{1i}\alpha_1^2+u_{2i}\alpha_2,\quad f_2=u_{3i}\alpha_1^2,$$
$$f_3=u_{4i}\alpha_2\alpha_1+u_{5i}\alpha_1,\quad f_4=u_{6i}\alpha_2\alpha_1+u_{7i}\alpha_1,\quad i=Pa,Si,Ci \tag{28}$$

where

$$u_{1i}=\frac{1}{32A_{22}^{*}}\left(\frac{nL}{\pi am}\right)^2,\quad u_{2i}=\frac{4B_{21}^{*}\pi^2m^2a-L^2}{8A_{22}^{*}am^2\pi^2},\quad u_{3i}=\frac{1}{32A_{11}^{*}}\left(\frac{ma\pi}{nL}\right)^2,$$

$$u_{4i}=-\frac{(\pi mLan)^2}{A_{22}^*(m\pi a)^4+A_{11}^*(nL)^4+T_1(L\pi anm)^2},$$

$$u_{5Si}=-\frac{B_{12}^*L^4n^4-2\pi^2a^2L^2\left(n^2L^2HI_{1Si}-0.5\left(-a+\delta_2n^2\right)m^2\right)+B_{21}^*(m\pi a)^4}{A_{22}^*(m\pi a)^4+A_{11}^*(nL)^4+T_1(L\pi anm)^2},$$

$$I_{1Si}=\int_0^L\left(\sin\left(\frac{\pi mx}{L}\right)\right)^2\sin\left(\frac{\pi x}{L}\right)\left(\left(\cos\left(\frac{\pi x}{L}\right)\right)^2\pi^2H^2+L^2\right)^{-3/2}\mathrm{d}x,$$

$$u_{5Pa}=\frac{16Hn^2a^2L^7I_{1Pa}-\pi^4m^4a^4B_{21}^*-B_{21}^*L^4n^4-a^2\pi^2\left(n^2T_2-a\right)m^2L^2}{A_{22}^*(\pi ma)^4+A_{11}^*(Ln)^4+T_1(La\pi nm)^2},$$

$$I_{1Pa}=\int_0^L\frac{1}{\left(16(L-2x)^2H^2+L^4\right)^{3/2}}\left(\sin\left(\frac{m\pi x}{L}\right)\right)^2\mathrm{d}x,$$

$$u_{5Ci}=\frac{\left(-Rn^4B_{21}^*+a^2n^2\right)L^4-(m\pi a)^4RB_{21}^*-R(ma\pi)^2\left(n^2T_2-a\right)L^2}{R\left(A_{22}^*(m\pi a)^4+A_{11}^*(nL)^4+T_1(L\pi anm)^2\right)},$$

$$u_{6i}=\frac{(L\pi nma)^2}{81A_{22}^*(\pi ma)^4+9(Lnm\pi a)^2T_1+A_{11}^*L^4n^4},$$

$$u_{7Si}=\frac{2HL^4n^2\pi^2a^2I_{2Si}}{81(m\pi a)^4A_{22}^*+L^4n^4A_{11}^*+9T_1(L\pi anm)^2},$$

$$I_{2Si}=\int_0^L\sin\left(\frac{m\pi x}{L}\right)\sin\left(\frac{3m\pi x}{L}\right)\sin\left(\frac{x\pi}{L}\right)\left(\left(\cos\left(\frac{x\pi}{L}\right)\right)^2\pi^2H^2+L^2\right)^{-3/2}\mathrm{d}x,$$

$$u_{7Pa}=\frac{16Hn^2a^2L^7I_{2Pa}}{81A_{22}^*(m\pi a)^4+A_{11}^*n^4L^4+9T_1(L\pi anm)^2},$$

$$I_{2Pa}=\int_0^L\frac{1}{\left(16H^2(L-2x)^2+L^4\right)^{3/2}}\sin\left(\frac{3m\pi x}{L}\right)\sin\left(\frac{m\pi x}{L}\right)\mathrm{d}x,\quad u_{7Ci}=0.$$

The circumferential closed condition is written in the following form

$$\int_0^{2\pi a}v_{,y}\mathrm{d}y\mathrm{d}x=\int_0^L\int_0^{2\pi a}\left(\varepsilon_{0y}-\frac{w_{,y}^2}{2}+\frac{w}{a}\right)\mathrm{d}y\mathrm{d}x=0. \tag{29}$$

From Eq. (29), the expression $\sigma_{0y}$ can be found as

$$\sigma_{oy}=J_{2i}\alpha_1^2+J_{1i}\alpha_2+J_{3i}\alpha_0,\quad i=Pa,Si,Ci, \tag{30}$$

where

$$J_{1i}=\frac{1}{2ahA_{22}^*},\quad J_{2i}=-\frac{n^2}{8hA_{22}^*a^2},\quad J_{3i}=\frac{1}{hA_{22}^*a}.$$

The strain energy of the shell and the work done by the external loads are defined as

$$U_{in}=\frac{1}{2}\int_{-\frac{h}{2}}^{\frac{h}{2}}\int_0^{2\pi a}\int_0^L\left[\sigma_x\varepsilon_x+\sigma_y\varepsilon_y+\sigma_{xy}\gamma_{xy}\right]\mathrm{d}x\mathrm{d}y\mathrm{d}z,\quad U_{ext}=\int_0^{2\pi a}\int_0^L qw\mathrm{d}x\mathrm{d}y. \tag{31}$$

Substituting Eqs. (11), (14), (17) and (25) into Eq. (31), we have

$$\begin{aligned}U_{in}&=p_{1i}\alpha_0^2+p_{2i}\alpha_0\alpha_1^2+p_{3i}\alpha_0\alpha_2+p_{5i}\alpha_1^4+p_{6i}\alpha_1^2+p_{9i}\alpha_1^2\alpha_1^2+p_{10i}\alpha_1^2\alpha_2+p_{0i}\alpha_1^2,\\U_{ext}&=2qL\pi a\alpha_0+qL\pi a\alpha_2,\end{aligned} \tag{32}$$

where

$$p_{0i} = -\frac{T_3\pi^3 n^2 m^2 u_{5i}}{4La} + \frac{\pi\left(A_{22}^*(m\pi a)^4 + A_{11}^*(nL)^4 + T_1(L\pi anm)^2\right)u_{5i}^2}{4L^3a^3} + \frac{\pi\left(\left(B_{21}^* - X_{12}\right)a^4m^4\pi^4 + n^4L^4\left(B_{12}^* - X_{21}\right)\right)u_{5i}}{4a^3L^3} - \frac{\pi^5 S_{11}am^4}{4L^3} - \frac{\pi S_{22}Ln^4}{4a^3} - \frac{S_{66}\pi^3n^2m^2}{aL} - \frac{\pi^3n^2m^2S_{12}}{4La} + 2\pi h^2aLA_{22}^*J_{4i}J_{2i} + \frac{\pi a_7^2\left(81(m\pi a)^4A_{22}^* + 9T_1(L\pi anm)^2 + A_{11}^*(nL)^4\right)}{4L^3a^3} - \frac{\pi^3n^2m^2S_{21}}{4La}, \quad T_3 = \left(X_{11} + X_{22} - T_2 - 2X_{66}\right),$$

$$p_{1i} = A_{22}^*h^2aL\pi J_{3i}^2, \quad p_{2i} = 2A_{22}^*h^2\pi aLJ_{2i}J_{3i}, \quad p_{3i} = 2aA_{22}^*\pi Lh^2J_{1i}J_{3i},$$

$$p_{5i} = \frac{\pi\left(8A_{22}^*(am\pi)^4u_{1i}^2 + A_{22}^*L^4h^2a^4J_{2i}^2 + 8n^4A_{11}^*L^4u_{3i}^2\right)}{a^3L^3},$$

$$p_{6i} = \frac{\pi a\left(4\pi^4\left(2A_{22}^*u_{2i}^2 - S_{11}/2 + \left(X_{12} - B_{21}^*\right)b_{2i}\right)m^4 + A_{22}^*J_{1i}^2L^4h^2\right)}{L^3},$$

$$p_{9i} = \frac{\left(9u_{6i}^2 + u_{4i}^2\right)A_{66}^*m^2n^2\pi^3}{4aL} + \frac{m^2\left(9u_{6i}^2 + u_{4i}^2\right)A_{12}^*n^2\pi^3}{4aL} + \frac{L\left(u_{6i}^2 + u_{4i}^2\right)\pi n^4A_{11}^*}{4a^3} + \frac{m^4\left(81u_{6i}^2 + u_{4i}^2\right)a\pi^5A_{22}^*}{4L^3} + \frac{m^2\left(9u_{6i}^2 + u_{4i}^2\right)A_{21}^*n^2\pi^3}{4aL},$$

$$p_{10i} = \frac{1}{2}\frac{\pi u_{7i}\left(L^4A_{11}^*n^4 + 81A_{22}^*(ma\pi)^4 + 9T_1(L\pi anm)^2\right)u_{6i}}{L^3a^3} + \frac{16\pi^5am^4A_{22}^*u_{2i}u_{1i}}{L^3} + \frac{1}{2}\frac{\pi u_{5i}\left((ma\pi)^4A_{22}^* + T_1(L\pi anm)^2 + L^4A_{11}^*n^4\right)u_{4i}}{L^3a^3} + \frac{1}{4}\frac{\pi n^4L^4\left(-X_{21} + B_{12}^*\right)u_{4i}}{a^3L^3} + 2A_{22}^*\pi aLh^2J_{2i}J_{1i} + \frac{\pi^5m^4a\left(16X_{12} - 16B_{21}^*\right)u_{1i}}{4L^3} + \frac{1}{4}\frac{\pi u_{4i}\left(m^4\left(B_{21}^* - X_{12}\right)a^4\pi^4 - (L\pi anm)^2T_3\right)}{L^3a^3}.$$

The total potential energy of the stiffened shell is expressed by

$$U_{Total} = U_{in} - U_{ext}. \tag{33}$$

The Ritz energy method is then applied as

$$\frac{\partial U_{Total}}{\partial\alpha_0} = \frac{\partial U_{Total}}{\partial\alpha_1} = \frac{\partial U_{Total}}{\partial\alpha_2} = 0. \tag{34}$$

From Eq. (34), the expression can be obtained as

$$2p_{1i}\alpha_0 - 2L\pi aq + p_{2i}\alpha_1^2 + p_{3i}\alpha_2 = 0, \tag{35}$$

$$2p_{5i}\alpha_1^2 + p_{9i}\alpha_2^2 + p_{10i}\alpha_2 + p_{2i}\alpha_0 + p_{0i} = 0, \tag{36}$$

$$L\pi aq + 2p_{9i}\alpha_1^2\alpha_2 + p_{10i}\alpha_1^2 + p_{3i}\alpha_0\alpha_2 + 2p_{6i}\alpha_2^2 = 0. \tag{37}$$

The expression of $\alpha_0$ can be found from Eq. (35)

$$\alpha_0 = \frac{2L\pi aq - p_{2i}\alpha_1^2 - p_{3i}\alpha_2}{2p_{1i}}. \tag{38}$$

Substituting Eq. (38) into Eq. (37), the expression of $\alpha_1^2$ can be obtained as

$$\alpha_1^2 = \frac{q_{4i}\alpha_2 + q_{3i}q}{q_{1i}\alpha_2 + q_{2i}}, \quad i = Pa, Si, Ci, \tag{39}$$

where

$$q_{1i} = -4p_{1i}p_{9i}, \; q_{2i} = p_{2i}p_{3i} - 2p_{10i}p_{1i}, \; q_{3i} = 2a\pi L\left(p_{3i} - p_{1i}\right), \; q_{4i} = 4p_{1i}p_{6i} - p_{3i}^2.$$

Substituting Eqs. (38), (39) into Eq. (36), the relation between $q$ and $\alpha_2$ is obtained as

$$q = \frac{q_{7i}\alpha_2^3 + q_{8i}\alpha_2^2 + q_{9i}\alpha_2 + q_{10i}}{2L\pi a q_{2i}q_{1i}\alpha_2 + q_{6i}}, \quad i = Pa, Si, Ci, \tag{40}$$

where

$$\begin{aligned}
&q_{6i} = q_{3i}\left(4p_{1i}p_{5i} - p_{2i}^2\right) + 2aL\pi p_{2i}q_{2i}, \quad q_{7i} = -2p_{9i}q_{1i}p_{1i},\\
&q_{8i} = -2\left(p_{10i}q_{1i} + p_{9i}q_{2i}\right)p_{1i} + p_{3i}p_{2i}q_{1i},\\
&q_{9i} = 2p_{1i}\left(-p_{0i}q_{1i} - p_{10i}q_{2i}\right) - 4p_{1i}p_{5i}q_{4i} + p_{2i}^2q_{4i} + p_{2i}p_{3i}q_{2i},\\
&q_{10i} = 2 - p_{0i}p_{1i}q_{2i}.
\end{aligned}$$

The maximal deflection expression can be obtained from Eq. (25) as

$$W = \alpha_0 + \alpha_1 + \alpha_2. \tag{41}$$

Substituting Eqs. (38), (39) into Eq. (41), the expression can be written as

$$W = \frac{1}{2p_{1i}}\left[2L\pi aq - \frac{p_{2i}\left(q_{4i}\alpha_2 + q_{3i}q\right)}{q_{1i}\alpha_2 + q_{2i}} - p_{3i}\alpha_2\right] + \alpha_2 + \sqrt{\frac{q_{4i}\alpha_2 + q_{3i}q}{q_{1i}\alpha_2 + q_{2i}}}. \tag{42}$$

The $q - W$ postbuckling curves of shells can be obtained by varying the nonlinear amplitude $\alpha_2$ and combining Eqs. (40) and (42).

By applying $\alpha_2 \to 0$, the buckling pressure of the shell segments is obtained, as

$$q_{buck} = \frac{q_{10i}}{q_{6i}}. \tag{43}$$

The critical buckling pressure $q_{cr}$ is defined to be the smallest buckling pressure with various buckling modes $(m, n)$.

## 4. VALIDATION OF THE RESULT

Table 1 compares the critical buckling loads obtained in the present study with those of Baruch and Singer (1963), Dung and Hoa (2013), and Shen (1997) for the perfect isotropic cylindrical shell with and without stiffeners under external pressure. The comparison shows that the present results are in good agreement with the existing results.

*Table 1.* Comparison of critical buckling loads (Psi) for isotropic cylindrical shells with and without stiffeners under external pressure

| Shell types | Shen (1997) | Baruch & Singer (1963) | Dung & Hoa (2013) | Present |
|---|---|---|---|---|
| Unstiffened | 100.7 (1, 4) | 102 | 103.3271 (1, 4) | 103.327 (1, 4) |
| Meridional stiffeners | 102.2 (1, 4) | 103 | 104.4937 (1, 4) | 104.494 (1, 4) |
| Circumferential stiffeners | 368.3 (1, 3) | 370 | 379.6944 (1, 3) | 379.431 (1, 3) |
| Orthogonal stiffeners | 374.1 (1, 3) | 377 | 387.1920 (1, 3) | 386.934 (1, 3) |

## 5. INVESTIGATION AND DISCUSSION

Table 2 shows the effect of the stiffener system and GPL distribution on the critical buckling pressure of porous core FG-GPLRC toroidal shell segments. As can be seen, the critical buckling loads of unstiffened FG-GPLRC shells are lower than those of stiffened FG-GPLRC shells. In both cases of stiffened shells and unstiffened shells, the critical buckling loads of FG-O shells are the lowest, and those of FG-X shells are the highest. Orthogonal stiffeners help the shell to withstand loads more effectively than circumferential or meridional stiffeners. Clearly, at the same rise $H$, the half-sinusoid toroidal shell segments have a larger load-carrying capacity than those with a parabolic configuration.

*Table 2*. The effect of stiffeners and GPL distribution on the critical buckling pressure $q_{cri}$ (MPa) of shells ($h = 2$ mm, $a = 100h$, $n_S = 50$, $n_R = 12$, $L = 2\pi a n_R / n_S$, $h_{Core} = 0.4h$, $W^*_{GPL} = 0.5\%$, $e_0 = 0.2$, $h_S = b_S = h$)

| Type | FG-X | UD | FG-O |
|---|---|---|---|
| Circular toroidal shell segments $R = 2.844$ m | | | |
| Unstiffened | 1.632 (1, 8) | 1.493 (1, 8) | 1.346 (1, 8) |
| Meridional stiffeners | 1.643 (1, 8) | 1.505 (1, 8) | 1.358 (1, 8) |
| Circumferential stiffeners | 2.382 (1, 7) | 2.248 (1, 7) | 2.102 (1, 7) |
| Orthogonal stiffeners | 2.400 (1, 7) | 2.265 (1, 7) | 2.119 (1, 7) |
| Parabolic toroidal shell segments ($H = 2h$) | | | |
| Unstiffened | 1.632 (1, 8) | 1.493 (1, 8) | 1.346 (1, 8) |
| Meridional stiffeners | 1.643 (1, 8) | 1.505 (1, 8) | 1.358 (1, 8) |
| Circumferential stiffeners | 2.383 (1, 7) | 2.248 (1, 7) | 2.102 (1, 7) |
| Orthogonal stiffeners | 2.400 (1, 7) | 2.266 (1, 7) | 2.119 (1, 7) |
| Half-sinusoid toroidal shell segments ($H = 2h$) | | | |
| Unstiffened | 1.653 (1, 8) | 1.513 (1, 8) | 1.365 (1, 8) |
| Meridional stiffeners | 1.666 (1, 8) | 1.526 (1, 8) | 1.378 (1, 8) |
| Circumferential stiffeners | 2.415 (1, 7) | 2.278 (1, 7) | 2.131 (1, 7) |
| Orthogonal stiffeners | 2.434 (1, 7) | 2.297 (1, 7) | 2.149 (1, 7) |

Table 3 presents the influence of the total mass fraction of GPLs $W^*_{GPL}$ on the critical buckling pressure of stiffened shells. The results show that increasing the GPL mass fraction from 0.1% to 0.5% leads to a consistent and noticeable increase in the critical buckling pressure for all material distributions (FG-X, UD, and FG-O) and for both shell geometries (parabolic and half-sinusoid). This indicates that the addition of GPLs effectively enhances the buckling resistance of the shells.

Fig. 2 compares the postbuckling curves of three types of shells in the case of an unstiffened convex shell. As observed, all three postbuckling curves follow a similar trend. The postbuckling curve of the half-sinusoid toroidal shell segment demonstrates a slightly higher load-carrying capacity than the other two shell types in the small deflection region. Fig. 3 indicates the effect of stiffeners on the postbuckling curve of half-sinusoid toroidal shell segments with a porous core. The general trend of all curves is similar; however, the curve of the unstiffened shell shows the lowest load-carrying capacity among all cases. Adding meridional stiffeners improves the buckling resistance compared to the unstiffened shell, but the enhancement provides modest improvement. The effectiveness of circumferential stiffeners is considerably greater than that of meridional stiffeners; however, orthogonal stiffeners are the most effective in enhancing structural stability.

*Table 3.* The effect of the total mass fraction of GPLs $W^*_{GPL}$ on the critical buckling pressure $q_{cri}$ (MPa) of shells ($h = 2$ mm, $a = 100h$, Orthogonal stiffener, $n_S = 50$, $n_R = 12$, $L = 2\pi a n_R / n_S$, $h_{Core} = 0.4h$, $e_0 = 0.2$, $h_S = b_S = h$)

| Type | FG-X | UD | FG-O |
|---|---|---|---|
| Parabolic toroidal shell segments ($H = 3h$) | | | |
| $W^*_{GPL} = 0.1\%$ | 2.260 (1, 7) | 2.226 (1, 7) | 2.192 (1, 7) |
| $W^*_{GPL} = 0.3\%$ | 2.516 (1, 7) | 2.420 (1, 7) | 2.320 (1, 7) |
| $W^*_{GPL} = 0.5\%$ | 2.760 (1, 7) | 2.608 (1, 7) | 2.443 (1, 7) |
| Half-sinusoid toroidal shell segments ($H = 3h$) | | | |
| $W^*_{GPL} = 0.1\%$ | 2.312 (1, 7) | 2.278 (1, 7) | 2.243 (1, 7) |
| $W^*_{GPL} = 0.3\%$ | 2.572 (1, 7) | 2.475 (1, 7) | 2.373 (1, 7) |
| $W^*_{GPL} = 0.5\%$ | 2.821 (1, 7) | 2.666 (1, 7) | 2.499 (1, 7) |

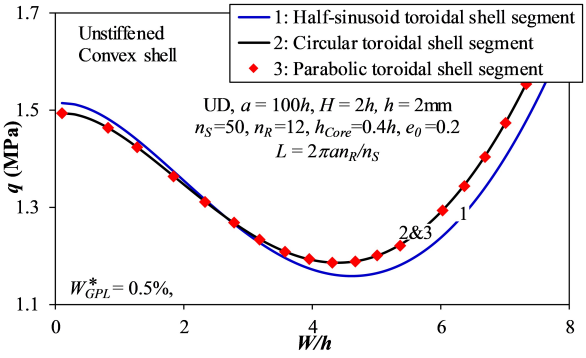


*Fig. 2.* Comparison of the postbuckling curves of Half-sinusoid, Parabolic, and Circular toroidal shell segments

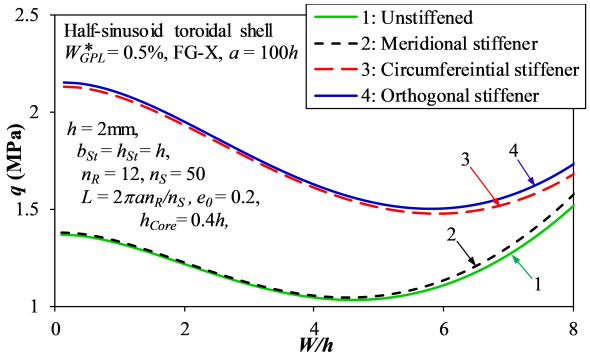


*Fig. 3.* Effects of the stiffeners on the postbuckling curves of Half-sinusoid, Parabolic, and Circular toroidal shell segments.

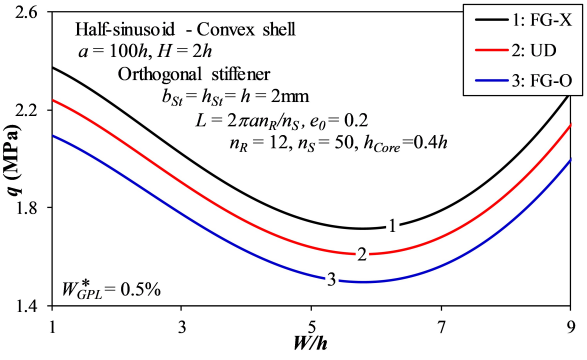


*Fig. 4.* Effects of GPL distributions on the postbuckling curves

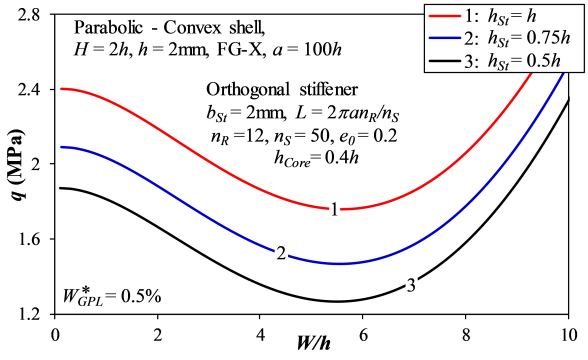


*Fig. 5.* The effect of stiffener height on the postbuckling curve

The effects of GPL distributions on the postbuckling curves of the orthogonally stiffened half-sinusoid convex shell are shown in Fig. 4. In general, the trends of curves and the snap-through intensities are unchanged with different GPL distributions. The FG-X configuration is the most effective, followed by the UD configuration, while the FG-O configuration provides the least resistance to buckling. The highest postbuckling strength of the shell is achieved with the FG-X configuration, suggesting that structural stability is significantly enhanced by this

GPL distribution. The effect of stiffener height on the postbuckling curves of the orthogonally stiffened parabolic convex shell is displayed in Fig. 5. It is evident that the impact of stiffener height on the structural performance of convex parabolic shells is significant. Higher stiffeners improve the load-carrying capacity and enhance the shell's postbuckling behavior.

Fig. 6 displays the effects of GPL mass fraction on the postbuckling curves of the orthogonally stiffened parabolic convex shell. Increasing the GPL mass fraction enhances the shell's stiffness and load-carrying capacity. This trend indicates that GPLs improve the overall structural performance, making the shell more resistant to external loads. Fig. 7 illustrates the effect of porous core thickness on the load-carrying capacity of an orthogonally stiffened half-sinusoid convex shell. A thicker porous core reduces the shell's stiffness and load-carrying capacity, even when the total shell thickness remains constant. In other words, reducing the thickness of the porous core enhances the structural performance in terms of strength.

Fig. 8 presents the effects of the rise $H$ on the postbuckling curves of a parabolic convex shell with FG-X distribution. As can be observed, an increase in the $H$ value will increase the critical load of the shell, and the postbuckling curves change significantly, as shown in the figure. Fig. 9 presents the effect of the geometric ratio $a/h$ on the postbuckling curves of half-sinusoid convex shells. An increased $a/h$ ratio will reduce the critical load and significantly change the postbuckling curve.

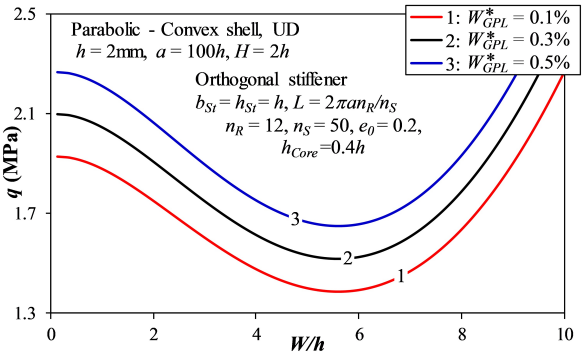


*Fig. 6.* Effects of the mass fraction of GPL on the postbuckling curves

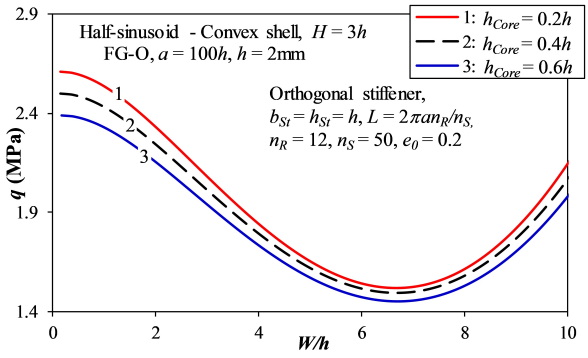


*Fig. 7.* Effects of the core thickness on the postbuckling curves

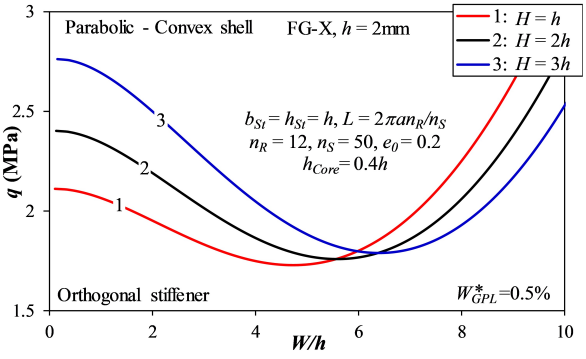


*Fig. 8.* Effect of the rise $H$ on the postbuckling curves

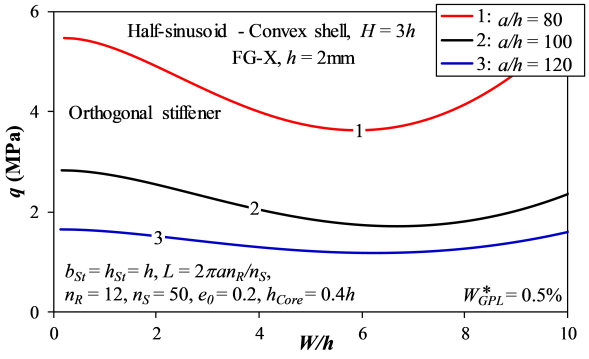


*Fig. 9.* Effects of the $a/h$ ratio on the postbuckling curves

## 6. CONCLUSIONS

This paper employed Donnell shell theory and von Kármán nonlinearity to develop an analysis of porous core stiffened FG-GPLRC toroidal shell segments with generalized meridional

curvature subjected to external pressure. A smeared stiffener technique is used to model the FG-GPLRC stiffeners, and the Ritz method is applied to obtain the expression for determining the critical load. Numerical results highlight the following significant effects:

(1) The half-sinusoid toroidal shell segment exhibits a higher load-carrying capacity than the parabolic and circular toroidal shell segments.

(2) Additionally, the critical buckling pressure of orthogonally stiffened shells is significantly higher than that of circumferentially or meridionally stiffened shells. The snap-through phenomenon is also clearly observed in all investigations.

(3) Among all considered distribution laws, the stiffened FG-X shell demonstrates the highest load-carrying capacity.

(4) An increase in the thickness of the porous core layer leads to a reduction in the shell's load-carrying capacity, even when the total shell thickness remains constant.

(5) In summary, increasing the rise $H$ improves the critical load, whereas a larger slenderness ratio $a/h$ weakens the load-carrying capacity of FG-GPLRC toroidal shells with orthogonal stiffeners.

## DECLARATION OF COMPETING INTEREST

The authors declare that they have no known competing financial interests or personal relationships that could have appeared to influence the work reported in this paper.

## CREDIT AUTHOR STATEMENT

Vu Hoai Nam: *Conceptualization, Methodology, Writing – original draft, Supervision*. Kieu Lan Huong: *Validation, Resources, Data curation*. Le Ngoc Ly: *Investigation, Data curation, Visualization*. Cao Van Doan: *Software, Investigation, Validation, Writing – review & editing*. Pham Thanh Hieu: *Formal analysis, Investigation*.

## ACKNOWLEDGEMENT

This research is funded by Vietnam National Foundation for Science and Technology Development (NAFOSTED) under grant number 107.02-2023.45.

## REFERENCES

Baruch, M., & Singer, J. (1963). Effect of eccentricity of stiffeners on the general instability of stiffened cylindrical shells under hydrostatic pressure. *Journal of Mechanical Engineering Science*, *5*(1), 23–27. https://doi.org/10.1243/jmes_jour_1963_005_005_02

Cheshmeh, E., Karbon, M., Eyvazian, A., Jung, D. w., Habibi, M., & Safarpour, M. (2020). Buckling and vibration analysis of FG-CNTRC plate subjected to thermo-mechanical load based on higher order shear deformation theory. *Mechanics Based Design of Structures and Machines*, *50*(4), 1137–1160. https://doi.org/10.1080/15397734.2020.1744005

Doan, C. V., Hung, V. T., Phuong, N. T., & Nam, V. H. (2022). Torsional buckling and postbuckling behavior of stiffened FG-GRCL toroidal shell segments surrounded by elastic foundation. *International Journal of Computational Materials Science and Engineering*, *12*(03), 2350001. https://doi.org/10.1142/s204768412350001x

Dung, D. V., & Hoa, L. K. (2013). Nonlinear buckling and post-buckling analysis of eccentrically stiffened functionally graded circular cylindrical shells under external pressure. *Thin-Walled Structures*, *63*, 117–124. https://doi.org/10.1016/j.tws.2012.09.010

Hieu, P. T., & Tung, H. V. (2020). Thermal and thermomechanical buckling of shear deformable FG-CNTRC cylindrical shells and toroidal shell segments with tangentially restrained edges. *Archive of Applied Mechanics*, *90*(7), 1529–1546. https://doi.org/10.1007/s00419-020-01682-7

Klecka, J., Cizek, J., Matejicek, J., Lukac, F., & Vala, J. (2023). Thick functionally-graded W-316L composite coatings for nuclear fusion applications. *Nuclear Materials and Energy*, *34*, 101373. https://doi.org/10.1016/j.nme.2023.101373

Minh, T. Q., Duc, V. M., Dong, D. T., & Nam, V. H. (2022). Nonlinear buckling analysis of higher-order shear deformable FG-CNTRC plates stiffened by oblique FG-CNTRC stiffeners. *Vietnam Journal of Mechanics*, *44*(4), 431–444. https://doi.org/10.15625/0866-7136/17933

Naj, R., Sabzikar Boroujerdy, M., & Eslami, M. R. (2008). Thermal and mechanical instability of functionally graded truncated conical shells. *Thin-Walled Structures*, *46*(1), 65–78. https://doi.org/10.1016/j.tws.2007.07.011

Nguyen, T. P., Vu, M. D., Cao, V. D., & Vu, H. N. (2021). Nonlinear torsional buckling of functionally graded graphene-reinforced composite (FG-GRC) laminated cylindrical shells stiffened by FG-GRC laminated stiffeners in thermal environment. *Polymer Composites*, *42*(6), 3051–3063. https://doi.org/10.1002/pc.26038

Phuong, N. T., Trung, N.-T., Van Doan, C., Thang, N. D., Duc, V. M., & Nam, V. H. (2020). Nonlinear thermomechanical buckling of FG-GRC laminated cylindrical shells stiffened by FG-GRC stiffeners subjected to external pressure. *Acta Mechanica*, *231*(12), 5125–5144. https://doi.org/10.1007/s00707-020-02813-5

Shen, H.-S. (1997). Post-buckling analysis of imperfect stiffened laminated cylindrical shells under combined external pressure and axial compression. *Computers & Structures*, *63*(2), 335–348. https://doi.org/10.1016/s0045-7949(96)00341-0

Shen, H.-S., & Noda, N. (2005). Postbuckling of FGM cylindrical shells under combined axial and radial mechanical loads in thermal environments. *International Journal of Solids and Structures*, *42*(16–17), 4641–4662. https://doi.org/10.1016/j.ijsolstr.2005.02.005

Shi, H., Zhou, P., Li, J., Liu, C., & Wang, L. (2021). Functional gradient metallic biomaterials: Techniques, current scenery, and future prospects in the biomedical field. *Frontiers in Bioengineering and Biotechnology*, *8*, 616845. https://doi.org/10.3389/fbioe.2020.616845

Wang, Y., Zeng, R., & Safarpour, M. (2020). Vibration analysis of FG-GPLRC annular plate in a thermal environment. *Mechanics Based Design of Structures and Machines*, *50*(1), 352–370. https://doi.org/10.1080/15397734.2020.1719508

Yadav, S., Liu, S., Singh, R. K., Sharma, A. K., & Rawat, P. (2024). A state-of-art review on functionally graded materials (FGMs) manufactured by 3D printing techniques: Advantages, existing challenges, and future scope. *Journal of Manufacturing Processes*, *131*, 2051–2072. https://doi.org/10.1016/j.jmapro.2024.10.026

Zhang, W., Wang, C., & Wang, Y. (2023). Thermo-mechanical analysis of porous functionally graded graphene reinforced cylindrical panels using an improved third order shear deformable model. *Applied Mathematical Modelling*, *118*, 453–473. https://doi.org/10.1016/j.apm.2023.01.026

Zhou, Z., Ni, Y., Tong, Z., Zhu, S., Sun, J., & Xu, X. (2019). Accurate nonlinear buckling analysis of functionally graded porous graphene platelet reinforced composite cylindrical shells. *International Journal of Mechanical Sciences*, *151*, 537–550. https://doi.org/10.1016/j.ijmecsci.2018.12.012